

Comparison of flame-front visualization in internal combustion engines using different imaging systems via endoscopic and full optical access

M. Goschütz*, S. Shawal, M. Schild, C. Schulz, S.A. Kaiser

Institute for Combustion and Gas Dynamics – Reactive Fluids, University of Duisburg-Essen, Germany

Abstract

Recently developed large-aperture UV endoscopes enable optical access with improved light collection in nearly unmodified production engines, operated at speeds and loads significantly exceeding the limits of most “optical” engines. In this study several different camera systems were used together with such an endoscopic system to image early flame-front propagation in spark-ignition engines. The camera systems were: “single-shot imaging” with an intensified CCD camera and “high-speed” cinematography with a CMOS-camera, both with and without an intensifier. As a reference “best-case scenario” serves unintensified high-speed imaging with a commercial camera lens in an engine with full optically access. We first visually compare the image quality produced by the different systems. Since a typical goal of such combustion visualization is to quantify the spatio-temporal features of early flame-front propagation, we then binarize the images and compare the flame progress as a function of crank angle.

Introduction

Flame front development, in particular with respect to cycle-to-cycle variability has been investigated previously by imaging of chemiluminescence (CL) from excited OH- and CH-radicals [1, 2] or sodium added to the fuel [3], by schlieren techniques [4], or by OH- and formaldehyde LIF [5, 6]. Some of these investigations show a strong correlation between the flame growth and pressure-derived heat release. Hence, flame-front imaging can be used as indication of reaction progress. However, in research engines with large-scale optical access less mechanical strength, reduced cooling, and altered thermal conductivity reduce the operating range in speed and load. Furthermore, the in-cylinder flow, with its influence on flame expansion and convective flame displacement, can be different from a production engine due to modifications needed to create optical access, for example, greatly increased crevice volumes.

The emphasis in endoscopic access, however, is on minimizing the impact on operating conditions, *i.e.*, keeping thermodynamics, heat transfer, and speed/load range as close as possible to that of an all-metal engine. Therefore, engines with endoscopic access never yield the same degree of freedom in terms of optical diagnostics. Additionally, most endoscopes employed for in-cylinder imaging were not originally designed for such use but are essentially modified medical instruments. Their light-collection efficiency is modest and most cannot be used in the ultraviolet (UV). This limits their use to processes generating much detectable light like Mie-scattering from sprays [7, 8] or flame luminosity and soot formation in diesel engines [8-12]. Also demonstrated were two-color visualization of 2-D soot luminosity to obtain the spatio-temporally resolved flame temperature [13, 14] and particle image velocimetry (PIV) [15], which are also techniques with relatively high levels of visible light.

The recent development of a UV-transparent endoscope with relatively large aperture [16] enables the detection of much weaker signals, like those from premixed combustion [17] or laser-induced fluorescence in the UV [18]. In this paper we compare premixed flame-front detection via different endoscopic techniques with measurements in an optical engine. The imaging systems are “single-shot” imaging with an intensified camera (ICCD) and “high-speed” cinematography with a CMOS-camera, both with and without an intensifier. As a reference “best-case scenario” serves unintensified high-speed imaging with a large-aperture commercial camera lens in an engine with full optical access via a quartz-glass cylinder. The data from intensified imaging (phase-locked and cinematographic) in the endoscopic engine were presented in a previous paper [17], while the data from unintensified imaging in both endoscopic and optical engine are new.

Experiments

Engines

Endoscopic imaging was performed in a production 4-cylinder engine from BMW (N46B20) with port-fuel injection, and a mechanically variable intake-valve train (“Valvetronic”). The latter also controlled the load by reducing the valve lift and opening duration in part-load operation. The engine speed was controlled by the dynamometer, while the load was set by an analogue input to the OEM engine control unit (ECU), which then determined all other parameters like fuel injection, ignition timing (IT), as well as valve lift and valve timings. It was not possible to actively change the ECU’s parameterization, but all relevant values could be read out. In the current work, the engine operated at 2000 min⁻¹ and 75 Nm, the maximum torque at that speed being 176 Nm.

* Corresponding author: martin.goschuetz@uni-due.de
Proceedings of the European Combustion Meeting 2015

Similar experiments were then also performed in a fully optically accessible single-cylinder gasoline engine (AVL) with a pent-roof four-valve head and a flat piston top. The engine was operated on premixed air/fuel charge, throttled to an intake pressure of 700 mbar. Additional throttling by reduced lift of the intake valves (3.0 mm) and the exhaust (3.5 mm) valves resulted in a part-load condition comparable to that used for the endoscopic experiments. Parameters and operation conditions for both optical and production engines are summarized in Table 1.

Engine	Endoscopic	Optical
Cylinders	4	1
Compression ratio		10
Displacement		499 cm ³
Bore		84 mm
Stroke		90 mm
Speed	2000 min ⁻¹	1500 min ⁻¹
Fuel		Iso-octane
Rel. fuel/air-ratio		1.0
Ignition timing	-34.5°CA	-45°CA

Table 1: Engines parameters and operating conditions

Endoscopic imaging systems

In the production engine, the main modifications to the engine were two additional ports in the fourth cylinder (by the gear box), creating optical access via two endoscopes with 10 mm diameter each, one for laser input (optional, not used here) and another for observation. To enable optical diagnostics in the full operating range of the engine, the front section of the endoscope was protected from the combustion chamber's pressure and temperature by a 3 mm-thick sapphire window, mounted in a titanium bushing with an outer diameter of 12 mm. A schematic drawing of the glass-liner and endoscopic imaging systems is shown in Figure 1.

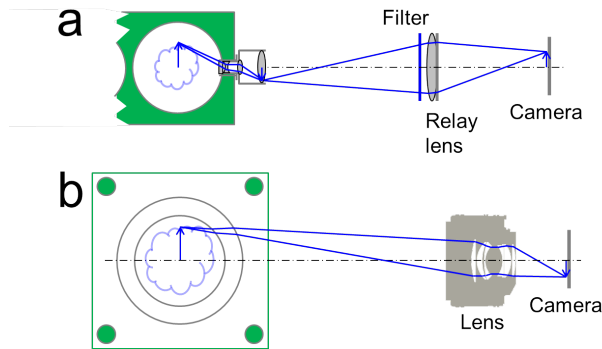


Figure 1 : Schematic diagram of (a) endoscopic and (b) glass-liner imaging system

The optical system utilized a two-stage concept. A front endoscope with wide-angle characteristics was mounted directly in the engine, creating an intermediate image on a field lens. The maximum angle of view was about 60°, yielding a field of view (FOV) with a diameter of about 40 mm in the center of the combustion chamber. All lenses in the endoscope were manufactured from UV-grade fused silica.

A relay optic, isolated from the vibrations of the engine, projected this intermediate image onto the camera. For imaging in the UV, the relay optic was a hybrid refractive-diffractive optical (R-DO) element, correcting the system's inherent chromatic aberration [16]. For imaging in the visible, a commercial camera lens was used instead to re-project the intermediate image. The system was designed in a previous project and is now commercially available from LaVision GmbH, Germany. With this endoscope system, imaging was carried out with three different camera systems, whose characteristics are summarized in Table 2.

Imaging system	Endo. SS-OH*	Endo. HS-OH*	Endo. HS-VIS	Optical HS-VIS
Camera type	ICCD	ICMOS	CMOS	CMOS
Rep. rate	10 Hz	6688 Hz	11019 Hz	18000 Hz
Exposure time	10 μs	20 μs	20 μs	15 μs
Spectral window	300 – 335 nm		400 – 800 nm	
Lens system	Hybrid R-DO		50 mm f/1.2	
Region of interest	520x688 pixels ²	800x600 pixels ²	608x456 pixels ²	512x312 pixels ²

Table 2: Main parameters of the imaging systems

Phase-locked single-shot imaging

In a first step, imaging of chemiluminescent hydroxyl radicals, OH*, was performed with an image-intensified CCD (S20 photocathode). OH* CL, mostly at 307 – 310 nm, is a proxy for the presence of high-temperature reactions. A band-pass filter in front of the relay optics blocked broadband radiation not stemming from OH*. 2 x 2 binning yielded a spatial discretization of 520 x 688 pixels. In a compromise between motion blur and signal level, the exposure time was set to 10 μs. Due to the low repetition rate of the ICCD, this camera system permits only one image acquisition per cycle, typically “phase-locked”, i.e., at the same crank-angle.

Intensified high-speed cinematography

In the “intensified high-speed” configuration, OH* visualization was performed with an active-pixel sensor CMOS camera (Phantom v7.3), lens-coupled to an image intensifier. The full array of 800 x 600 pixels was read out at a repetition rate of 6688 Hz, corresponding to one image per 1.794°CA at 2000 rpm. Based on pixel number, this detection scheme would be expected to yield better spatial resolution than phase-locked imaging, but in fact the high-speed image intensifier degrades the actual resolution much more than its low-repetition-rate counterpart, as will be seen in the results. The images were gated to have an exposure time of 20 μ, increasing light collection at the expense of potentially blurring the flame front.

Unintensified high-speed cinematography

This measurement was performed with the same CMOS camera, but without the intensifier and the band pass filter. The CMOS detector itself is most sensitive in

a spectral range between 400 and 800 nm. Such broadband sensing in the visible mainly detects the luminescent species CH^* , CO , CO_2 , and H_2O . These may not be directly associated with the flame front. A Nikon 50 mm, f/1.2 lens combined with a close-up lens (Canon 250D) relay-imaged the endoscopic FOV onto 608 x 456 pixels. Reducing the readout area of the detector increased the repetition rate to 11019 Hz (1.089°CA per image) at 2000 rpm.

Glass-liner imaging system

In the optical engine, the entire upper part of the cylinder was from quartz, which enabled viewing the pent-roof combustion chamber and the complete width of the bore to about 29 mm down from the fire deck. Again the CMOS-camera was used without intensifier and filter. The same commercial f/1.2-lens now directly projected the FOV onto 512 x 312 pixels. The exposure time was set to 15 μs . At 1500 rpm, the repetition rate of 18 kHz corresponds to one image per 0.5°CA .

Results and discussion

Example image series

Phase-locked single-shot imaging

Figure 2 shows the development of the flame for $6.0^\circ\text{CA} - 20^\circ\text{CA}$ aIT as a “pseudo flame propagation”, composed from separate cycles at the same operating condition. Consistent with imaging in optical engines [2, 6], the first flame kernel can be observed at around $5^\circ\text{CA} - 6^\circ\text{CA}$ aIT. This initial flame then grows towards the pent roof and spreads to the sides. Flame convection towards the intake valves (left) is consistent with the ignition spark bending to the left at 8°CA aIT. Flame growth is accompanied by an increase of intensity. At 20°CA aIT the flame had propagated close to the edge of the endoscope’s FOV.

By visual appearance, the noise and contrast of the images from this system are only slightly worse than those from earlier work with a similar imaging system applied to a fully optically accessible engine [1, 2].

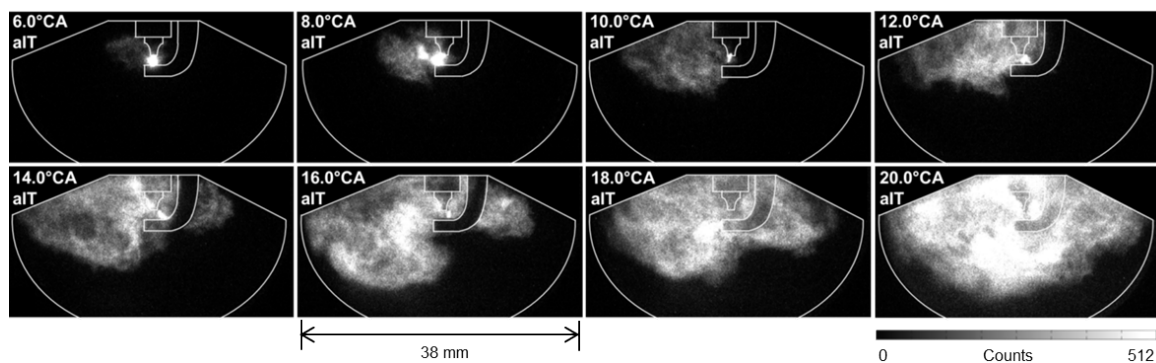


Figure 2: Endoscopic “phase-locked” single shot imaging of OH^* . Pseudo time-series composed of images from separate cycles at different crank angles after ignition timing (aIT).

Intensified high-speed cinematography

Figure 3 shows a series of OH^* CL images from intensified high-speed endoscopic imaging. Clearly the images in Figure 3 have less contrast and resolution than the corresponding images in Figure 2. To reach kHz repetition rates, compromises have to be made in the design of image intensifiers, and similarly CMOS cameras optimized for extremely fast read-out are noisier than “slow” CCD or CMOS detectors. In particular, the strong emission from the spark impacts parts of the image that are several millimeters away. The spark’s luminosity is probably in large parts not due to OH^* [2, 3], but other species that either emit within the transmission band of the filter or have emission strong enough to “leak” through the filter in its spectrally blocked range. A comparison with Figure 2 and Figure 4 suggests that the seemingly large spatial extent of the spark signal is solely due smearing by the high-speed image intensifier.

Despite the limited spatial resolution of the images, a few qualitative observations can be made. The delay between spark initialization and the onset of discernible flame propagation differs between the two sample sequences. In the first series during about the first 10°CA aIT only the spark can be seen, while in the

second one an irregularly-shaped flame emerges from the saturated part of the image at 5.6°CA aIT. Correspondingly, by the end of the second sequence the burned area fills a much greater portion of the FOV. Both series confirm a key finding of previous research, [1][3] that flames keep their shape while growing. The main direction of convective displacement in these sequences is evident as well and is different between the two sequences, a clear indication of significant cycle-to-cycle variability in the flow field near TDC.

Unintensified high-speed cinematography

Figure 4 shows two sequences from endoscopic unintensified high-speed cinematography. As opposed to the images in Figure 3 details of the spark are discernible here. Although the ignition event itself was not our primary interest here, much can be learned from imaging the spark channel [2, 3], therefore this could be a significant advantage over intensified imaging. The lack of an intensifier-induced “halo” means that the flame kernel can be distinguished from the spark earlier. However, without the analog amplification of the intensifier upstream of the CMOS-detector the signal is much closer to the read-out noise of the detector. Visible CL may also not be as strong as the UV-

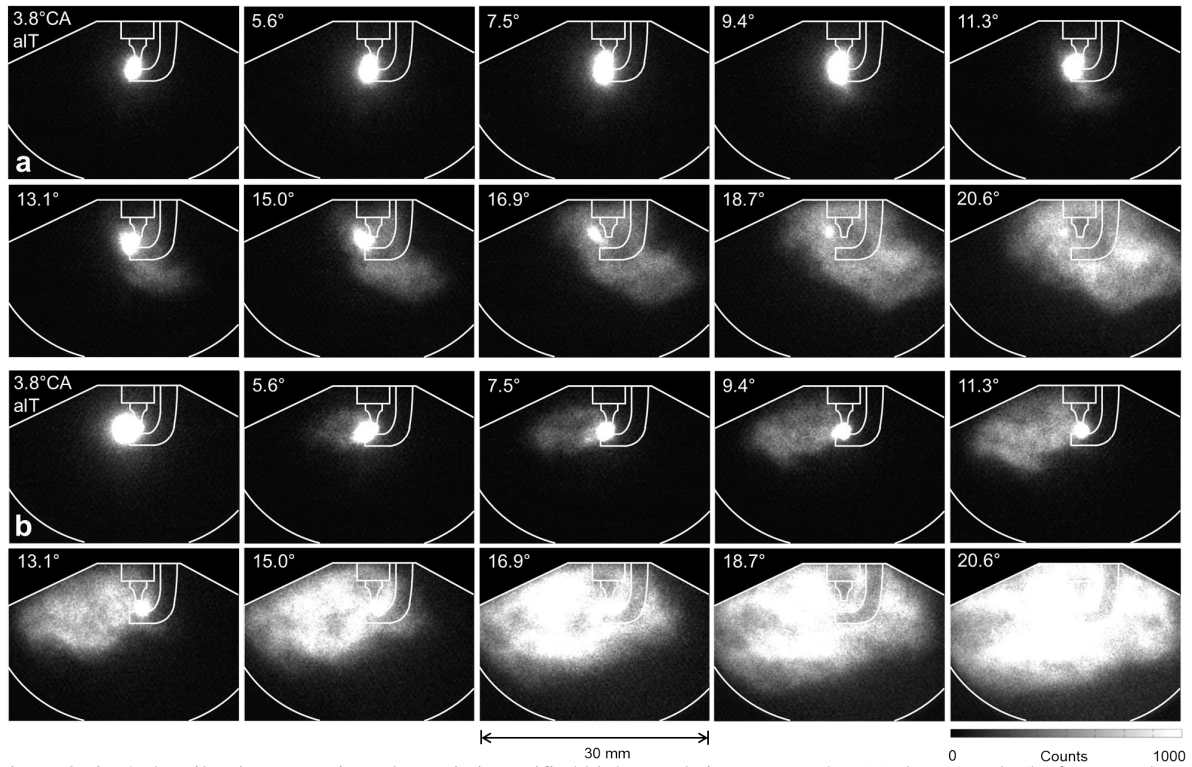


Figure 3: OH* chemiluminescence in endoscopic intensified high-speed cinematography: (a) slower cycle (b) faster cycle.

emission of OH*. This particular camera shows a pattern in the read-out noise that is spatially shifting with time. To obtain the lowest noise floor in those images that capture the weakly luminescent nascent flame kernel, we subtracted the mean of the last 10 images in each cycle before the spark from each subsequent image. This works quite well for the first

few crank angles after ignition, but later the pattern has shifted too much and cannot be fully compensated. As a result the edge of the burned area is “ragged”. For later crank angles, the increase in signal partially compensates the concurrent increase in background noise.

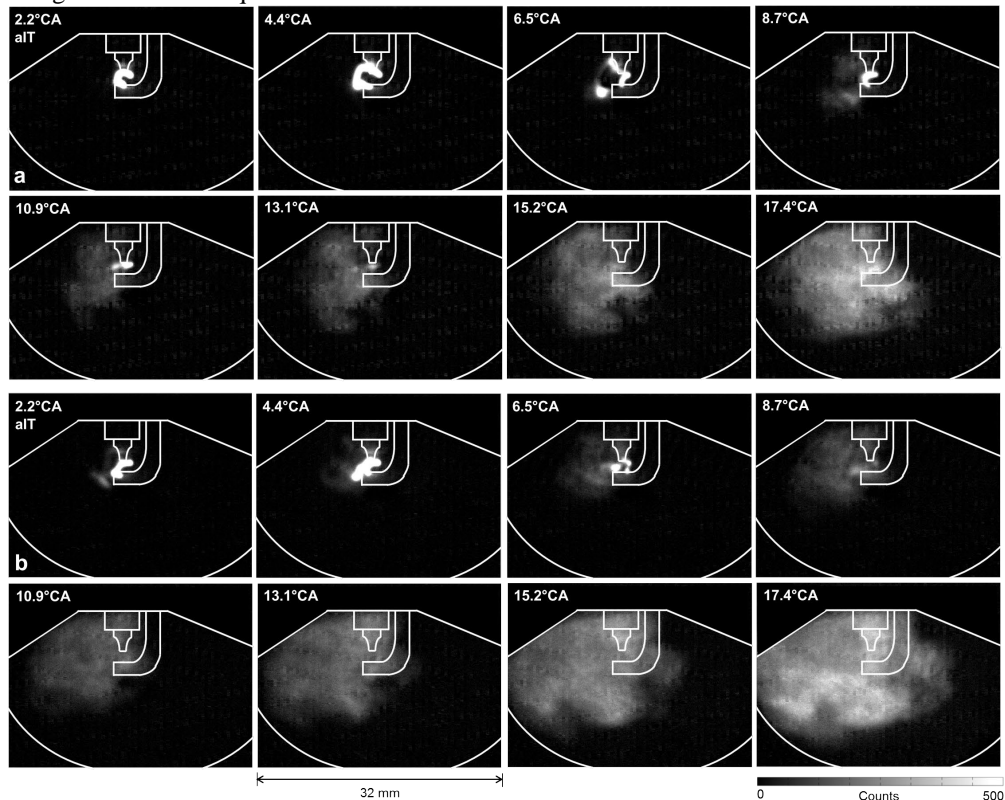


Figure 4: Endoscopic unintensified high-speed cinematography: (a) slower cycle (b) faster cycle.

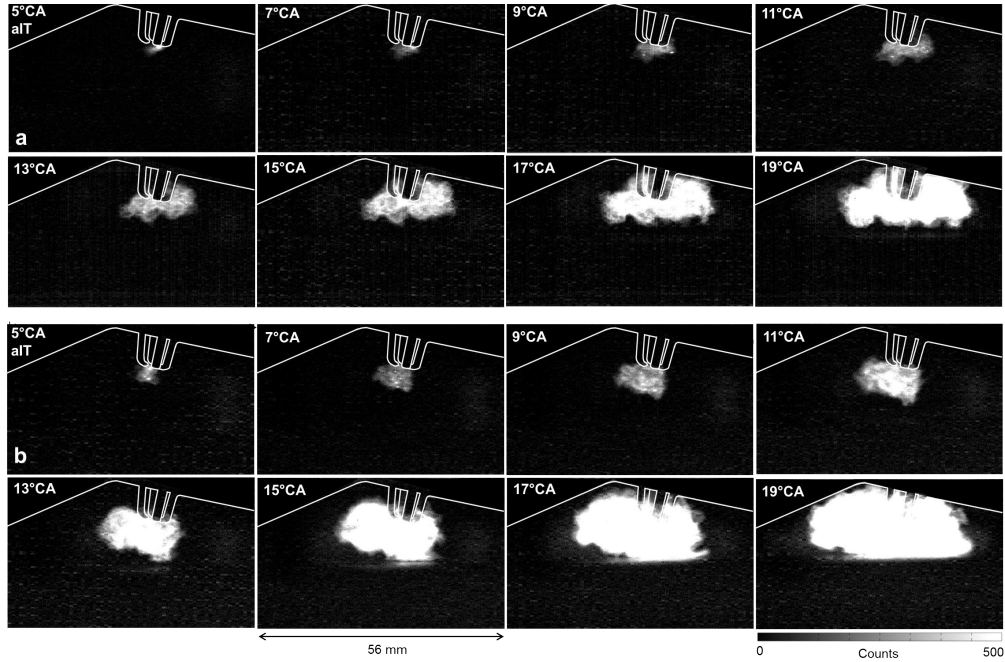


Figure 5: Unintensified glass-liner cinematography: (a) slower cycle (b) faster cycle. Note the wider FOV.

High-speed glass-liner cinematography

The image sequences in Figure 5 show the image quality that can be achieved when the optical access is nearly unrestricted. Despite even higher frame rate and thus reduced detector area, the detected signal is about twice as high. The images also appear sharper than those in Figure 4, but this is not necessarily due to better spatial resolution of the non-endoscopic imaging system, but rather because the read-out pattern is less important compared to the higher signal. Also, at the given reproduction size, the wider FOV gives the impression of a sharper image. The spatial features of are similar to those seen in the endoscopic production engine, but the three-prong spark plug in the optical engine seems to obscure the spark to a large extent.

Morphological image analysis

To derive quantitative spatial information on the propagation of the early flame front, the images were binarized by intensity-based segmentation. For the images from intensified endoscopic imaging (Figure 3 and 4) we took the flame areas from previous work [17]. In that work, the images were binarized by thresholding all images from a given crank-angle after ignition timing (aIT) at a fixed intensity value.

For the new data sets from unintensified high-speed cinematography we devised a different strategy to better account for cycle-to-cycle variability in CL intensity. Here, the threshold was automatically determined for each individual image based on a weighted average of the intensity in the current image and the previous image. The first image in each series was segmented via the histogram-based Otsu method [19]. Before binarization, the background was subtracted as described above and the images were filtered with a 5x5 pixel median filter to reduce the remaining noise.

Figure 7 presents the burned area as function of crank angle for all four combinations of engine and imaging system. While the cinematographic methods yield a trace for each cycle, data points from phase-locked imaging [17] are uncorrelated between cycles. Their multi-cycle mean is shown (dashed line).

All three plots in Figure 7 are similar in that mostly the burned area monotonically increases and the lines representing each cycle's flame-front progress do not cross. The former is physically reasonable and the latter has been observed before [1, 4, 6]. Imaging in the optical engine, Figure 7c, shows these finding most clearly. We therefore consider this the "correct" result.

Compared to this base line the intensified endoscopic measurement shown in Figure 7a has the most scatter at early crank angles. Many traces, also those of the highlighted cycles, cross. Also, in the mean, the flame area does not expand between 4 and 8°CA aIT, with many cycles showing a period of a seemingly receding flame. Inspection of the raw images indicates that for this part of the cycle the flame area is overestimated as consequence to the detector smearing out the saturated area caused by the spark's luminosity. After 8°CA aIT, scatter is reduced. The multi-cycle mean nearly matches the phase-locked mean from single-shot imaging.

In contrast, scatter from the unintensified endoscopic data in Figure 7b is more consistent over the measurement duration. Thus, compared to the intensified version the variance during early flame development is lower. This is because the spark causes only very local saturation of the detector. Again, the multi-cycle average roughly matches the phase-locked single-shot mean. The greater scatter at late crank angles (and compared to glass-liner imaging, Figure 7c, at all crank angles) shows the influence of the read-out noise pattern on edge detection.

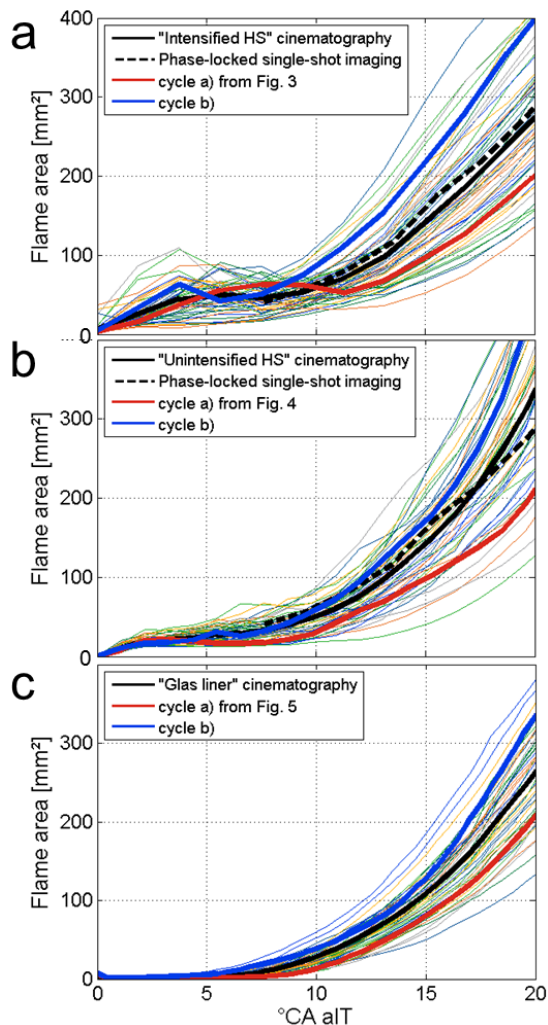


Figure 7: Flame area for 50 consecutive cycles (colored lines) and the multi-cycle mean of these 50 cycles (solid black line)

- Endoscopic intensified cinematography
- Endoscopic unintensified cinematography
- Glass-liner unintensified cinematography

Compared to the other two sub-figures, Figure 7c, representing data from the optical engine, shows markedly different traces for crank-angles before 8° aIT: the burned area smoothly increases from zero in the latter case, while the former two indicate non-zero values immediately after IT. The difference is due to the spark-plug geometry: the spark is mostly hidden by the three prongs of the optical engine's plug. This may be beneficial or detrimental, depending on the desired information. In the endoscopic methods it would be possible mask out the spark by placing a spatial filter (a black dot, in essence) onto the front endoscope's field lens, where a real intermediate image is formed.

Conclusions

Early flame-front propagation was investigated with a large-aperture UV endoscope in a nearly unmodified production SI engine. Three different imaging configurations were applied and compared with unintensified high-speed cinematography with a large-aperture camera lens in an engine with full optical access. The apparent flame area was derived by morphological post-processing.

In endoscopic imaging with its limited aperture (equivalent to $f/4.5$ [16]) single-shot intensified imaging of OH^* yielded the best images. However, the cinematographic techniques are much more attractive because they capture the history of each single cycle. Here, intensified imaging of OH^* has advantages and disadvantages compared to broadband detection in the visible with the unintensified CMOS sensor. In the former case, spatial "smearing" of the intensifier is a problem during the extremely bright spark event when blinds the detector in the vicinity of the spark.

Unfortunately, current high-speed CMOS cameras are not sensitive in the UV where $\text{OH}^*\text{-CL}$ provides a strong and spatially well-defined signal. However, even with that limitation, the large-aperture endoscope made the use of this detector feasible for the current task. The read-out noise pattern limits low-light performance. This may be overcome with hardware improvement or with more sophisticated post-processing.

Acknowledgements

This work was funded by the Rückkehrprogramm of the NRW Ministry for Innovation, Science, and Research, the Deutsche Forschungsgemeinschaft, project Schu 1369/12-1, and the Ministry of Education of Malaysia and Universiti Teknologi MARA (UiTM).

References

- P. G. Aleiferis, A. M. K. P. Taylor, K. Ishii, Y. Urata, *Combustion and Flame* 136 (2004) 283–302.
- P. G. Aleiferis, A. M. K. P. Taylor, J. H. Whitelaw, K. Ishii, Y. Urata, SAE Technical Paper 2000-01-1207 (2000)
- R. N. Dahms, M. C. Drake, T. D. Fansler, T.-W. Kuo, N. Peters, *Combustion and Flame* 158 (2011) 2229–2244.
- V. Salazar, S. A. Kaiser, SAE Technical Paper 2011-24-0098 (2011)
- R. Collin, J. Nygren, M. Richter, M. Aldén, L. Hildingsson, B. Johansson, SAE Technical Paper 2003-01-3218 (2003)
- S. H. R. Müller, B. Böhm, M. Gleißner, S. Arndt, A. Dreizler, *Applied Physics B* 100 (2010) 447–452.
- P. Sementa, B. M. Vaglieco, F. Catapano, *Fuel* 96 (2012) 204–219
- K. Schänzlin, T. Koch, K. Boulouchos, SAE Technical Paper 2002-01-0834 (2002)
- S. A. Miers, H. Ng, S. A. Ciatti, K. Stork, SAE Technical Paper 2005-01-3670 (2005)
- S.-C. Kong, L. M. Ricart, R. D. Reitz, SAE Technical Paper 950455 (1995)
- P. L. Mtui, P. G. Hill, SAE Technical Paper 961933 (1996)
- J. Eismark, M. Balthasar, A. Karlsson, T. Benham, M. Christensen, I. Denbratt, SAE Technical Paper 2009-01-2813 (2009)
- T. Shiozaki, H. Nakajima, Y. Kudo, A. Miyashita, Y. Aoyagi, SAE Technical Paper 960323 (1996)
- M. Bakenhus, R. D. Reitz, SAE Technical Paper 1999-01-1112 (1999)
- U. Dierksheide, P. Meyer, T. Hovestadt, W. Hentschel, *Experiments in Fluids* 33 (2002) 794–800.
- R. Reichle, C. Pruss, C. Gessenhardt, C. Schulz, W. Osten, *Applied Optics* 51 (12) (2012) 1982–1996.
- M. Goschütz, C. Schulz, S. A. Kaiser, *SAE Int. J. Engines* 7 (1) (2014) 351–365.
- C. Gessenhardt, C. Schulz, S. A. Kaiser, *Proceedings of the Combustion Institute* 35 (2015) 3697–3705.
- N. Otsu, *IEEE Transactions on Systems, Man, and Cybernetics SMC-9* (1) (1979) 62–66.